Sub-diffraction spatial mapping of nanomechanical modes using a plasmomechanical system

Brian J. Roxworthy[1], Sreya Vangara[2], and Vladimir A. Aksyuk[1,*]
[1] Center for Nanoscale Science and Technology, National Institute of Standards and Technology, Gaithersburg, MD 20899, USA
[2] Poolesville High School, Poolesville, MD 20837, USA
[*] Corresponding author: vladimir.aksyuk@nist.gov

Abstract
Plasmomechanical systems – formed by introducing a mechanically compliant gap between metallic nanostructures – produce large optomechanical interactions that can be localized to deep subwavelength volumes. This unique ability opens a new path to study optomechanics in nanometer-scale regimes inaccessible by other methods. We show that the localized optomechanical interactions produced by plasmomechanics can be used to spatially map the displacement modes of a vibrating nanomechanical system with a resolution exceeding the diffraction limit. Furthermore, we use white light illumination for motion transduction instead of a monochromatic laser, and develop a semi-analytical model matching the changes in optomechanical coupling constant and motion signal strength observed in a broadband transduction experiment. Our results clearly demonstrate the key benefit of localized and broadband performance provided by plasmomechanical systems, which may enable future nano-scale sensing and wafer-scale metrology applications.

Key Words: plasmomechanical systems, nanoelectromechanical systems, broadband optomechanical transduction, localized gap plasmons,

Introduction
Progress in motion measurement for micro and nano-mechanical systems enables advances in many fields. Indeed, the characteristics of diverse physical systems are usefully imprinted on mechanical vibrations, forming the basis for atomic force microscopy for imaging and materials characterization [1,2], precision mass and force detection [3,4], biological sensing [5], radiofrequency signal processing [6], and quantum engineering [7,8]. Improving device functionality often requires shrinking the physical size of mechanical transducers, thereby necessitating high-spatial resolution and low-noise readout of their motions [9–11]. Cavity optomechanical systems are especially well-suited for this task. By trapping light within a high-quality dielectric optical resonator, these devices extend the time and localize the physical space in which optical and mechanical modes interact. As a result, these devices can transduce motion with remarkably high sensitivity[12], in some cases at the fundamental limits imposed by quantum mechanics. [13]. However, in dielectric devices, localization of the optical energy is limited to a volume of approximately λ^3, where λ is the optical wavelength inside the medium. This diffraction limit constrains the ability to read nanoscale device motion at precisely specified locations, or to selectively enhance or suppress optical coupling to specific mechanical modes at the nanoscale. The need to selectively transduce weak mechanical signals from nanoscale regions motivates the design of new platforms that can access deeply sub-diffraction mode volumes.

The emerging class of plasmomechanical systems offers a solution. These devices take advantage of the ability of plasmonic resonators to confine light into nanometer-sized volumes. By introducing a moveable mechanical degree of freedom into the gap separating metallic structures, plasmomechanical systems can concentrate light-motion interactions into these small volumes, while simultaneously providing optomechanical coupling rates several orders of magnitude larger than dielectric systems [14–17]. A variety of geometries have been explored to take full advantage of these effects, including patterned, gold-coated silicon nitride membranes [15,16,18], homogenous gold devices [19–22], and monolithically fabricated gold-nitride structures[17,23]. To date, previous efforts have focused mainly on transducing thermal motion [16,17], achieving broad optical resonance tuning [23], or harnessing near-field optical or thermal forces to control nanomechanical dynamics[18,23,24]. However, specifically employing the high-spatial resolution of plasmomechanical transduction remains largely unexplored. Additionally, in most studies, single-wavelength lasers are used to probe devices, neglecting the potential benefit of broadband plasmonic modes for transduction. Utilizing the broadband response may allow for incoherent, white-light optomechanics [25].

In this Article, we show that plasmomechanical interactions can be used to spatially map the displacement modes of a vibrating mechanical system. Localized gap plasmonic resonators embedded into cantilever structures act as point-like transducers which report the mechanical response from an area ≈ 4.3× smaller than the diffraction limited focal spot. By collecting the mechanical spectra from a set of localized-gap plasmon resonators (LGPRs), we can accurately reconstruct the shapes of the first three flexural modes of the cantilever. We also show that a broadband laser source can be used to transduce the motion from each LGPR, effectively relaxing the constraint of a precisely tunable laser source commonly required to probe optomechanical systems. We develop a semi-analytical model for broadband transduction which accounts for changes in optomechanical transduction gain and matches experimental results. These results introduce a new functionality for plasmomechanical devices while expanding their versatility for applications in sensing and metrology.

Results and Discussion

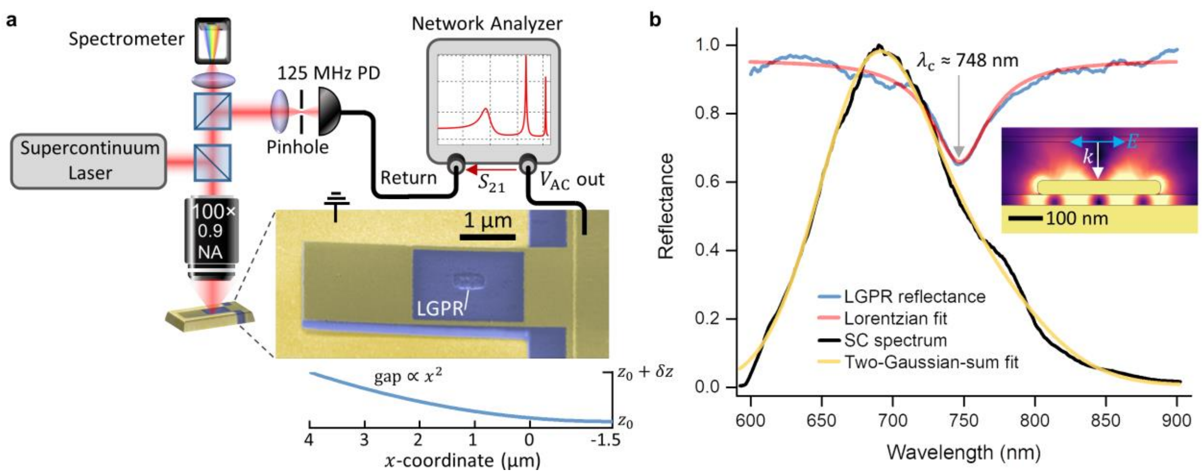

Figure 1. (a) Schematic of experimental setup. A supercontinuum (SC) laser supplies a broadband optical excitation focused to a ≈ 950 nm spot with a 0.9 NA objective. Reflected optical signals from the LGPR are passed onto a photodiode through a pinhole. A vector network analyzer drives the cantilever with ≈ 1 V signal and the transmission S_{21} is measured. The suspended cantilever (false-color scanning electron micrograph, inset) is separated from a large gold pad underneath by a quadratically increasing gap as fabricated, visible as the dark shadow under the cantilever. The embedded LGPR produces a visible bulge on the top cantilever surface. All experiments are performed in ambient air conditions. (b) The spectrum of the SC source (black), collected in reflection from the flat gold reflector next to the cantilever and the reflectance of a typical LGPR (blue). In the latter case, the background SC spectrum is first normalized by focusing on the cantilever ≈ 1 µm from the LGPR. The inset shows the electric field intensity distribution for the LGP mode with incident electric field (blue arrow) and wavevector (white arrow).

Our plasmomechanical system is based on an LGPR comprising a gold cuboid that measures approximately (350×150×40) nm^3 in length, width, and thickness, respectively. This structure represents a truncated metal-insulator-metal waveguide supporting a gap plasmon mode that is confined to the nanoscale gap below the cuboid [26]. The LGPR dimensions are chosen to produce a relatively high-quality factor localized gap plasmon (LGP) mode (Q ≈ 20) with a third-order resonance (Fig. 1b). This mode is primarily magnetic in character, exhibiting a magnetic dipole-like response directed orthogonal to the electric field polarization of the exciting laser beam [17]. The LGPR is suspended above an underlying gold substrate by embedding it on the underside of a free-hanging silicon nitride cantilever. The optical frequency (ω) response of the plasmon resonance dependes sensitively on the size z of the gap, yielding extremely large optomechanical interactions. The nominally 4 µm long, 150 nm thick silicon nitride cantilevers are attached to a ≈ 1.5 µm wide suspended frame and have a thin gold electrode patterned on their top surface to provide electrostatic actuation of their mechanical vibrations. The frame extends the total effective cantilever length to 5.5 µm and is included in our models. These devices are produced using a fabrication method previously described [23]. The false color scanning electron micrograph in Fig. 1a shows that the cantilevers are separated from the gold substrate by a gap that increases approximately parabolically toward the cantilever tip from an initial gap of ≈ 15 nm at the cantilever base and under the frame. The curvature is a result of the residual stress gradient in the nitride deposition process and can be controlled by varying process parameters (see Methods). Generally, decreasing the initial gap requires larger stresses to facilitate the release of the cantilevers and avoid stiction. Larger stress gradient leads to larger curvature, increasing cantilever-substrate gap along the cantilever length[23]. Six independent devices are studied, each having a single LGPR positioned at a location (x-coordinate) ranging nominally from 0.5 µm to 1.75 µm from the base with the cantilever and LGPR long dimensions oriented along x.

The experimentally measured optical response of a typical LGPR is shown in Fig. 1b. This reflectance spectrum is measured in a confocal arrangement, whereby a broadband supercontinuum (SC) is focused onto the LGPR to a diffraction-limited spot with a high-numerical aperture (0.9 NA) and the collected light is imaged onto a fiber-coupled spectrometer (Fig. 1a). The spectrum of the SC source, which is well-represented by a sum of two Gaussian functions (yellow curve, Fig. 1b), is normalized to a flat reference prior to measuring the LGPR response by focusing through the cantilever at the gold pad surface a small ≈ 1 µm distance away from the LGPR. The LGPR imparts a dip in the reflectance spectrum, near which we fit to a Lorentzian given by

$$r(\lambda) = R_0 + M\frac{w^2}{4(\lambda-\lambda_c)^2+w^2}, \tag{1}$$

where R_0 is the reflectance far from resonance, M is the coupling depth, w is the optical cavity linewidth (full-width at half maximum, FWHM), and λ_c is the LGP resonance wavelength (frequency, $\omega_c = 2\pi c/\lambda_c$, where c is the speed of light). The fit produces an LGP resonance with $\lambda_c \approx$ 748 nm, $M \approx$ 0.3, and $w \approx$ 49 nm.

To elucidate the nature of the optomechanical coupling of the system, we perform finite element calculations of the LGPR optical response as a function of the gap size z using the same geometry and dimensions of the fabricated devices. Figure 2a shows the calculated reflectance spectra for gaps spanning from 7.5 nm to 50 nm. These curves qualitatively match the Lorentzian form of the resonance observed in experiment, and we find close quantitative agreement between measured and calculated responses for z ranging from 20 nm to 30 nm. The LGPR exhibits both dispersive and reactive optomechanical coupling [23,27–29]. The dispersive component is characterized by changes in the resonance frequency with gap $g_{\mathrm{om}} = \partial\omega_c/\partial z$ and is strongest in the small-gap region below ≈ 20 nm with values in excess 2 THz nm^{-1}. In contrast, the reactive component derives from changes in both the modulation depth $\partial M/\partial z$ and the linewidth $\partial w/\partial z$ of the LGP, and dominates in the large gap regions above ≈ 35 nm, where the dispersive component becomes small.

Using these simulation data, we can construct a semi-analytical model for predicting the optomechanical transduction behavior of the devices. To build the model, we fit the FEM derived spectra $r(\lambda)$ to a series of Lorentzian curves, and extract the resonance wavelength, linewidth, and modulation depth at each gap (Fig. 2b-d). We then plot each fit parameter over the gap range and fit the resultant values to a set of phenomenological models. Figure 2b shows the extracted resonance wavelengths, which exhibit a well-known exponential dependence on gap $\lambda_c(z) = \lambda_0 + A_\lambda \exp[-z/\ell_\lambda]$ [30]. Similarly, the linewidth, representing the plasmonic losses, is expected to be large at small gaps due to significant electric field penetration into the metal, and to decrease as the gap becomes large [26]. We therefore fit the linewidth to an exponential form $w(z) = w_0 + A_w \exp[-z/\ell_w]$ (Fig. 2c). There is an apparent hybridization of the LGP with another mode for gaps near 20 nm. This mode is likely a dielectric loaded surface plasmon: a propagating surface plasmon excited by the LGPR and coupled to the nitride cantilever, which forms a dielectric waveguide [17]. The hybridization increases the apparent linewidth for gaps ≈ 20 nm (red diamond, Fig. 2c). Inversely, the modulation depth approaches zero at vanishing gap and is expected to reach a limiting value for large gaps. This suggests a power-law model of the form $M(z) = a_M - b_M\, c_M^z$ shown in Fig. 2d. We note that the deviations of $w(z)$ and $M(z)$ for gaps smaller than ≈ 20 nm are not expected to contribute significantly to the optomechanical transduction, due to the fact that dispersive coupling significantly outweighs reactive in this regime [23,27,29]. The deviations of $M(z)$ in this regime and the anomalously large gap value at 20 nm are therefore neglected in the fitting procedure in favor of a simplified model. Table 1 shows the derived fit parameters for each component along with their R^2 values which indicate the goodness of fit of each model value. Uncertainties in Table 1 are one-standard deviation from the fits.

Table 1. Fit parameters for semi-analytical $R(\lambda, z)$ model

$\lambda_c(z)$		$w(z)$		$M(z)$	
λ_0	(752±0.4) nm	w_0	(32±0.2) nm	a_M	0.46±0.04
A_λ	(326±20.5) nm	A_w	(233 ± 68) nm	b_M	0.49±0.06
ℓ_λ	(6.3±0.3) nm	ℓ_w	(3.1 ± 0.3) nm	c_M	0.94±0.02
R^2	0.99	R^2	0.84	R^2	0.91

Incorporating the model functions into Eq. (1) produces an analytical function of the reflectance

$$R(\lambda, z) = R_0 + M(z)\frac{w^2(z)}{4[\lambda - \lambda_c(z)]^2 + w^2(z)}, \qquad (2)$$

which is plotted in Fig. 2e. The utility of this construction is that the model enables direct calculation of the optomechanical transduction signal

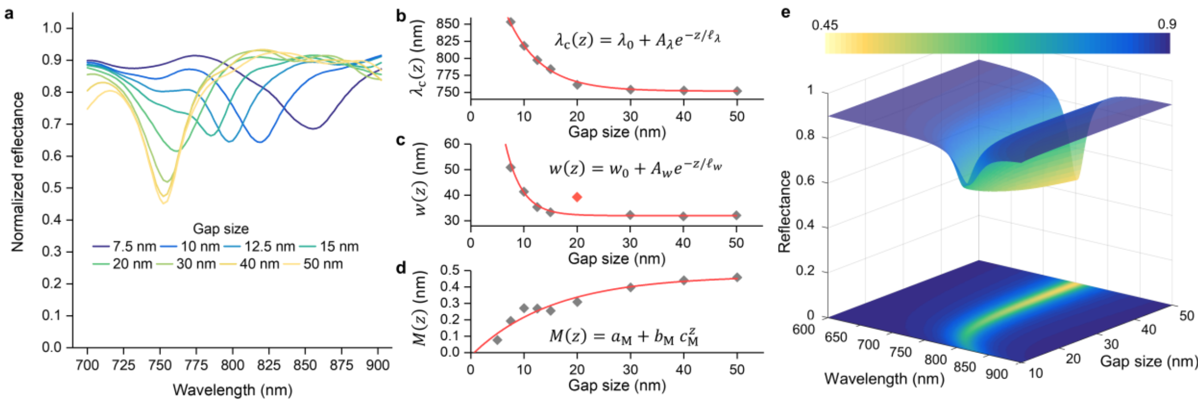

Figure 2. (a) Finite-element calculated reflectance spectra for LGPRs with varying gap sizes. (b)-(d) Extracted parameters from Lorentzian fits to (a) (gray diamonds) and their model functions (red lines). The red diamond in (c) is excluded from the fit. (e) Surface plot of the constructed analytical reflectance function $R(\lambda, z)$ using the models in (b)-(d). The bottom plane is a contour map of the three-dimensional surface.

$$s(\lambda, z) \propto \frac{\partial R(\lambda,z)}{\partial z}. \tag{3}$$

Commonly, optomechanical motion transduction is performed with a single-wavelength laser probe tuned near the cavity resonance of the device. In dielectric cavity optomechanics, this scheme is often required, as many of these systems have large optical quality factors that are deliberately engineered to improve transduction sensitivity, at the expense of decreased optical bandwidth [12,25]. Plasmomechanical systems, by contrast, have large intrinsic bandwidth and therefore the single-wavelength approach to transduction is not an a-priori requirement, despite being employed in most studies to date. Despite having a low quality factor compared to dielectric devices, plasmomechanical systems can still achieve transduction with a large signal-to-noise ratio owing to their exceptionally large optomechanical coupling strength; the signal being proportional to the $Q \cdot g_{\mathrm{om}}$ product [17].

We utilize a broadband optical source – the supercontinuum laser – for plasmomechanical transduction of device motion. This approach has several advantages. Presently, it enables monitoring the reflectance spectrum of the LGPR (Fig. 1) simultaneously with motion transduction, facilitating spatial alignment of the laser with the subwavelength resonator. The laser's high spatial coherence allows us to locate and characterize the nanoscale LGPR with the high spatial resolution of confocal microscopy. In the future, optically-broadband transduction may allow parallel, wide area (e.g. wafer-scale) metrology of plasmomechanical devices with varied optical resonances using incoherent illumination.

To account for broadband transduction, we use Eq. (3) and find

$$\mathcal{S}(z) = \int_{\lambda_0}^{\lambda_f} s(\lambda, z) \cdot SC(\lambda) \cdot \xi(\lambda) \, \mathrm{d}\lambda, \tag{4}$$

where $SC(\lambda)$ is the supercontinuum spectrum ranging from $\lambda_0 \approx 600$ nm to $\lambda_f \approx 900$ nm (Fig. 1b), and $\xi(\lambda)$ is the normalized responsivity of the photodiode Fig. 1a. In our devices, the LGPRs are placed at varying positions (x-coordinates) along the cantilever length and therefore sample different regimes of optomechanical coupling, owing to the curled shape of the released cantilever which is modeled by $z(x) = z_0 + \frac{\delta z}{L^2} x^2$ with cantilever length L, initial gap z_0, and deflection at the tip δz [31]. As a result, a reduction of the optomechanical coupling strength with increasing x-coordinate (gap) is expected.

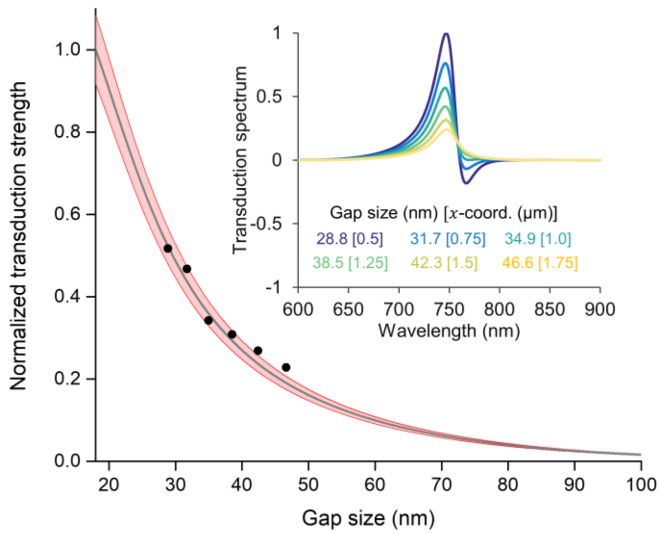

Figure 3. Broadband optomechanical transduction signal for the plasmomechanical system. The gray line is the result predicted from Eq. (4), using an initial gap of 18 nm and a tip deflection (gap at the tip) of 82 nm (100 nm) and the black circles derive from experimental measurements. The red region represents one standard-deviation propagated from uncertainties in the fit to the SC spectrum and from the standard deviation ($\pm$ 4 nm) of measured LGPR resonance wavelengths. The inset shows the individual transduction spectra $s(\lambda, z_i)$ where z_i are the predicted gaps for the six devices in our study.

Figure 3 shows the normalized transduction signal calculated using Eq. (4). The decrease in transduction strength due to the cantilever curvature is evident. In fact, we find that for a 4 μm length cantilever with a gap at the base (tip) of 18 nm (100 nm), corresponding to δz = 82 nm, the predicted relative transduction strength for the LGPRs closely matches experimental results (shown later). These static cantilever shape parameters used in the model agree with the parameters from the fabricated devices. In particular, the initial gap is taken from the deposited sacrificial layer thickness and the tip deflection value from atomic force microscopy measurements [23]. These measurements, performed on a different sample produced in the same fabrication run as the present set of devices, indicate an approximately 10 % variation of the tip deflection value across all devices. We expect and account for this variation in the six devices studied in this work. The spectra (inset, Fig. 3) show a transition from dispersive to purely reactive optomechanical coupling for gaps larger than ≈ 35 nm. Interestingly, this model reveals that broadband transduction using a dispersive device requires either an asymmetry in the source spectrum or an appreciable reactive coupling component. Without such asymmetry, the opposite phase (negative value) of the transduction spectrum cancels the positive part leading, in principle, to a vanishing signal.

The optomechanical transduction mechanism is most sensitive to motion that directly changes the gap size. Thus, the flexural modes of the cantilever will couple strongly to the LGPR, which probes the motion from a localized region smaller than the input laser spot size. We make use of this effect to spatially map the first three flexural modes of the cantilever (Fig. 4b) using the setup shown in Fig. 1a. Here, a vector network analyzer supplies a radio-frequency (rf) voltage from 1 MHz to 125 MHz to the electrostatic actuator, driving device motion and producing a modulated LGPR reflectance signal $S(z)$ which is read out using a 125 MHz bandwidth photodiode.

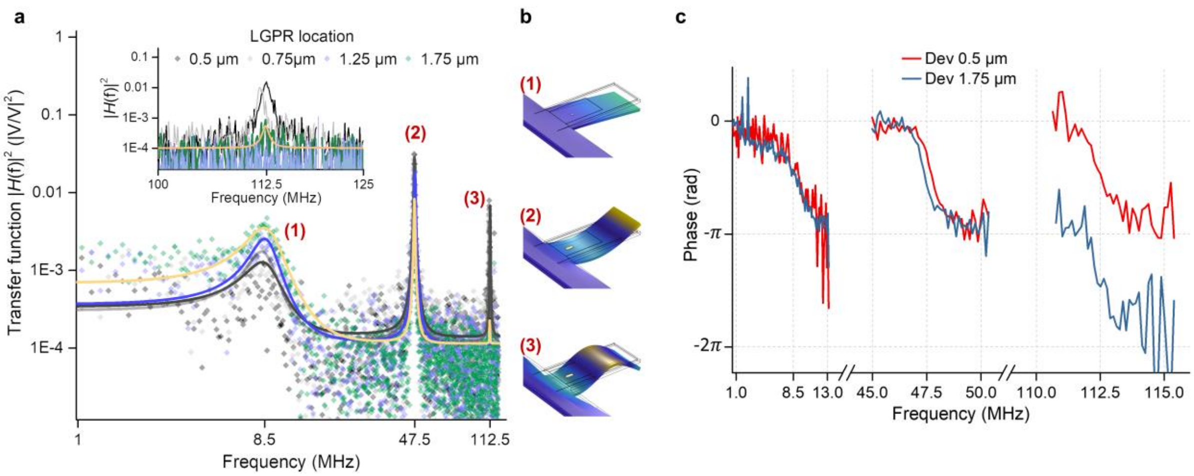

Figure 4. Transduced mechanical modes. (a) Power spectral density (PSD) of the mechanical frequency response of four devices plotted on a dual logarithmic scale with LGPRs located 0.5 µm (black), 0.75 µm (gray), 1.25 µm (blue), and 1.75 µm (green) from their respective cantilever bases. The inset is a zoom-in of mode 3. Solid curves are fits to Eq. (5) for each device. (b) Finite-element calculated modal displacement at each frequency $f_{\mathrm{m},j}$. (c) Phase of the transduced mode signals for 0.5 µm (red) and 1.75 µm (blue) devices.

Figure 4a shows the squared amplitude of the mechanical frequency transfer functions $|H(f)|^2$ of four representative devices transduced by the SC source. These curves, proportional to the power spectral density (PSD) of the mechanical vibrations, show peaks at the frequencies of the first three flexural modes – referred to as modes one, two, and three, respectively – of the cantilevers. The PSD is represented as a three-peaked Lorentzian function of the form

$$S_{zz,j}(\omega) = \left|\sum_j^3 \chi_j(\omega)\right|^2 S_{FF}(\omega) \approx S_{FF} \sum_j^3 \frac{1}{m_j^2} \frac{1}{\left(\omega_{\mathrm{m},j}^2 - \omega^2\right)^2 + \left(\gamma_{\mathrm{m},j}\,\omega\right)^2}, \tag{5}$$

where the index j refers to the mechanical mode, S_{FF} is the (flat) force spectral density of the electrostatic actuation, and $\chi_j(\omega)$ is the complex mechanical susceptibility with modal mass m_j, frequency $\omega_{\mathrm{m},j} = 2\pi\, f_{\mathrm{m},j}$, damping rate $\gamma_{\mathrm{m},j}$, and quality factor $Q_{\mathrm{m},j} = \omega_{\mathrm{m},j}/\gamma_{\mathrm{m},j}$. Given that there is no frequency overlap between the modes, the mechanical frequency response is effectively the incoherent sum of the three. The fit of Eq. 5 to the data (tan curve, Fig. 4a) includes a constant offset accounting for noise in the transduced signals. The mechanical frequencies, determined from Lorentzian fits to the full set of six devices, are (8.54 ± 0.52) MHz, (47.5 ± 0.02) MHz, and (112.5 ± 0.54) MHz, for modes one, two, and three (j =1, 2 and 3), respectively; uncertainties are the standard deviation of the average of the six devices. While the values for modes two and three agree with finite-element calculations to within 2 %, the $f_{\mathrm{m},1}$ is significantly larger than the predicted value of 7.2 MHz. We attribute this difference to squeeze film air interaction, which is not included in the finite element model and is expected to both stiffen and damp the mechanical response at low frequencies[32]; the deviation from the Lorentzian fit at low frequency is also expected as a result this effect.

The mechanical responses in Fig. 4a bear distinct signatures suggesting that the LGPR transduces mechanical motion locally. For mode one, there is monotonically increasing motion power with x-coordinate, whereas mode two shows little change in power. In contrast, mode three displacement signal is non-monotonic, displaying a distinct node for locations near x = 1.25 μm and a recovery of the signal for larger x positions. These observations agree qualitatively with the calculated mode shapes of the cantilever (Fig. 4b). Furthermore, the node in mode three implies that the displacement should exhibit opposite phase for locations on either side. The measured phase response (Fig. 4c) of the devices indeed shows a phase reversal for mode three whereas modes one and two retain the same phase for each device.

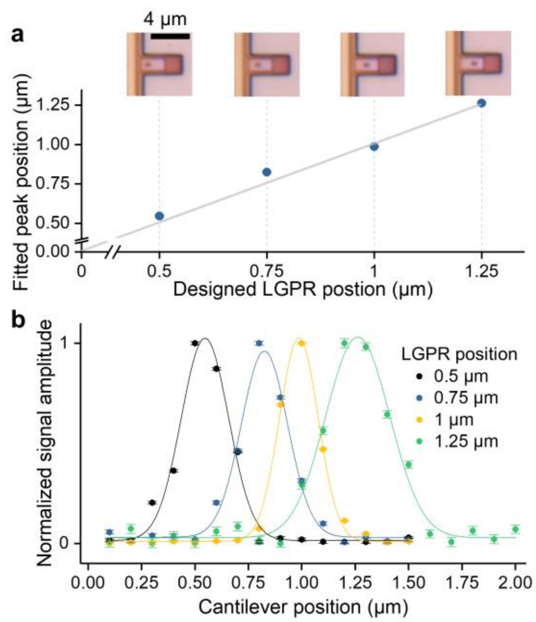

Figure 5. Spatially resolved motion signals. (a) Center positions of the (b) spatially dependent motion signals for the four devices shown in the optical micrographs. Values in (a) are the center positions extracted from Gaussian fits to the data in (b), with uncertainties that are one standard deviation propagated from the fit; error bars are much smaller than the data points. Error bars in (b) represent one standard deviation of the signal amplitude, propagated from a separate Gaussian fit to the motion signal data. Data in (b) are normalized such that the maximum signal value for each device is one.

These observations suggest that the LGPR indeed acts as a localized motion transducer, as previously suggested for plasmomechanical systems [16,17]. To further corroborate this point, we measure the mechanical response of mode two as the input laser is scanned along the cantilever length. For this measurement, we supply a 47.5 MHz tone to drive the mode, measure the motion signal amplitude at each location, and fit the spatially resolved signal amplitudes to a Gaussian function of laser position with ≈ 100 nm increments across the laser scan range. Given that (1) the lens used for excitation and detection has a high numerical aperture, and (2) the LGPR responds as a magnetic dipole with its moment along the y-axis (orthogonal to the input electric field polarization), it is expected from diffraction theory that the point-spread function of the imaged LGPR is elongated parallel to the y-axis [33]. Consequently, and somewhat counterintuitively, we expect to achieve better optical localization in x, parallel to the longer physical axis of the LGPR.

The extracted center positions from the fit for each device agree very well with the designed values for the LGPR locations within the cantilevers (Fig. 5a). Note that the fabrication process results in a maximum variation in the device-to-device LGPR position of ≈ 4 nm. Comparing this value to the minimum resolution of our wide-field microscope of ≈ 475 nm, we find that the signal is localized to a region that is ≈ 1.6× smaller than the diffraction limit. A similar comparison can be made to a confocal imaging system, wherein the minimum resolution is given by $0.37\lambda_{\mathrm{SC,peak}}/\mathrm{NA}$ ≈ 288 nm. Thus, the measured motion signal localization (Fig. 5b) corresponds closely to the theoretical confocal resolution limit given by $0.37\,\lambda_{\mathrm{SC,peak}}/\mathrm{NA} \approx 288$ nm, indicating that the LGPR is acting effectively as a point transducer of nanomechanical motion.

The point-like transduction provided by the LGPRs can be used to map out the mechanical mode shapes. To perform the mapping, we fit the mechanical spectra in Fig. 4a to Eq. 5 for six LGPR locations x_l from 0.5 µm to 1.75 µm in 250 nm increments; l is the LGPR location index from one to six. The fits are then used to derive the raw modal displacement via [34]

$$z_j(x_l) \propto \sqrt{\int_0^{\infty} S_{zz,j}(\omega)\mathrm{d}\omega}\,. \tag{6}$$

Finally, an error-weighted nonlinear fit of the raw $z_j(x_l)$ values to finite-element calculated mode shapes is performed. The fitting procedure takes as input the eighteen $z_j(x_l)$ values with their associated uncertainties, defined as the one-standard deviation uncertainty propagated from the Lorentzian fit, and uses two types of fit parameters to define the output. The first is a force gain factor g_j^{f}, comprising one value for each mode *j* =1,2,3, that accounts for the fact that the electrostatic actuator does not excite each mode with equal strength. Applying g_j^{f} effectively shifts the vertical positions of the raw $z_j(x_l)$. A second transduction gain factor g_l^{g} comprises six values, one for each LGPR location. These parameters account for the change in the optomechanical coupling strength with gap size $z(x_l)$. The results are shown in Fig. 6. We find an excellent agreement between measured and theoretical mechanical mode shapes. The extracted g_l^{g} (black circles, Fig. 3a) agree very well with theoretical predictions for optomechanical transduction (which assumes the parabolic cantilever shape), up to a common proportionality constant. Conversely, combining the experimentally determined g_l^{g}

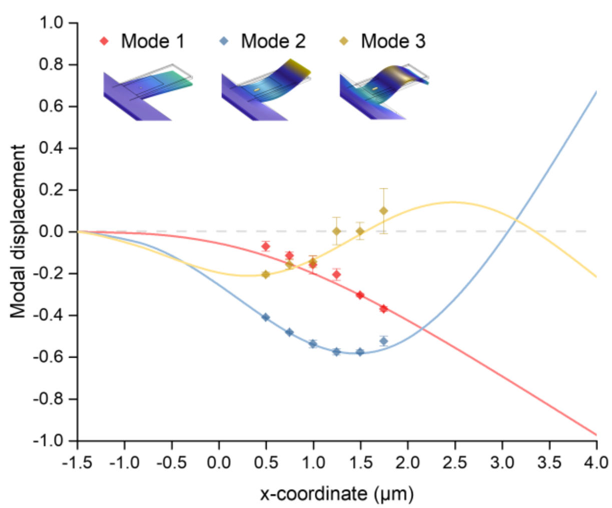

Figure 6. Normalized modal displacement values (diamonds) resulting from an error-weighted fit to finite-element calculated mode shapes (lines). The error bars represent uncertainties propagated from the nonlinear fit of the raw $z_j(x_l)$ to theoretical mode shapes and an additional 10 % uncertainty resulting from the variation in the cantilever tip deflection across all devices.

with the theoretical transduction model enables reconstruction of the curved equilibrium cantilever shape. Figure 7 shows the gap values, corresponding to the experimental transduction gains g_l^{g}, extracted from the $\mathcal{S}(z)$ curve. Indeed, we find that these values match the expected parabolic gap profile of the deflected cantilever.

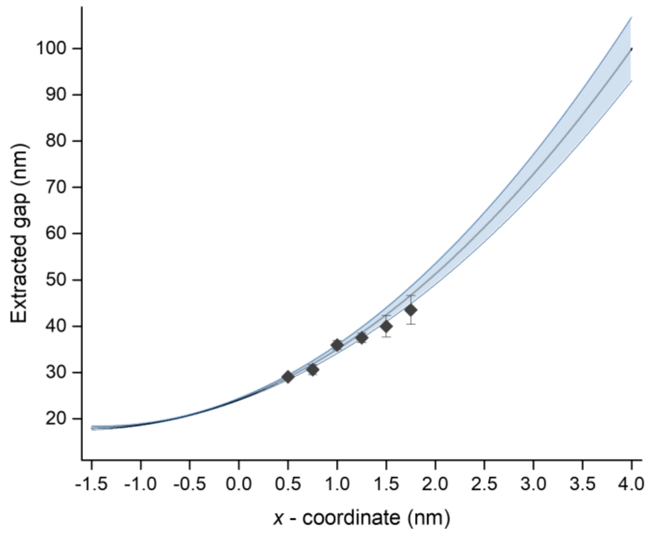

Figure 7. Gap size extracted (gray diamonds) through a combination of the experimental transduction gains and the theoretical broadband model. Error bars are the difference between the transduction gains and theoretical curve. The gray line is a parabola fit to the extracted gaps, with the blue region representing one standard deviation of the fit.

The reduction of optomechanical coupling strength with larger gap along the cantilever length, a direct result of the stress-induced deflection shown in Fig. 7, appears to limit the lateral extent over which the modes can be mapped. However, this is a consequence of the specific device parameters used in this work and is not a general limitation of the plasmomechanical mode mapping scheme. In order to produce and study LGPRs that sample both the dispersive and reactive regimes, it is necessary to fabricate narrow ≈ 15 nm initial gaps. Wet-etching release and supercritical CO_2 drying of such devices are more reliable with large film stress gradients, producing a large δz. When mode mapping is the only goal, it can be done entirely in the reactively coupled regime, whereby a larger initial gap can be used, easing the constraints on the stress required for device release, reducing δz, and ultimately extending the measurable lateral extent of the nanomechanical modes.

In the current implementation, the use of a single plasmonic element within each separate device is not only sufficient to map the nanomechanical modes, but also enables straightforward assessment of the sub-diffraction optical footprint of the motion transduction (Fig. 5). A natural extension of this technique is to employ multiple LGPRs in a single device. This method would allow the modes of individual devices to be mapped in one or two spatial dimensions, potentially revealing non-idealities in the dynamics of surface-machined NEMS devices. However, in such an approach, it is important to retain sufficient spacing between the plasmonic elements to prevent LGPR optical coupling. Finite element calculations show that LGPRs can be spaced as close as 100 nm without introducing significant coupling effects such as a shift in the LGP resonance frequency. Along these lines, an interesting future avenue would be to use smaller first-order resonators, measuring approximately 75 nm and 40 nm in length and width, respectively. These LGPRs support the first-order LGP mode in the same spectral range and may improve the spatial resolution and enable transduction of mechanical signals at sub 100 nm length scales and GHz frequencies.

While the large $Q \cdot g_{\mathrm{om}}$ product of the LGPRs contributes to a high sensitivity of the optomechanical readout, it is also important to maximize the number of photons (optical power) used for measurement to ensure a large signal-to-noise ratio (SNR). For plasmonic systems, the heat generated can be a limiting factor for the maximum optical power and therefore the achievable transduction SNR, as morphological changes can occur at temperatures as low as 200 °C [35,36]. With this temperature representing a conservative estimate of the structural damage threshold, we use a finite element model to calculate the maximum temperature of the LGPR and thus the likelihood of thermal damage. In our experiments, an input optical power of ≈ 5 mW (distributed over the full source bandwidth) is used, leading to a total dissipation of ≈ 100 μW over the LGPR bandwidth and a calculated maximum temperature of ≈ 70 °C, significantly below the damage threshold. We calculate that a maximum broadband input power of 20 mW can be used prior to damage. Assuming that photon shot noise is the primary noise source [17], this 4× increase of input power could improve the transduction SNR by a factor of two.

Conclusion

In summary, we have demonstrated new functionalities for plasmomechanical systems: high-spatial resolution mapping of the vibrational modes of a nanomechanical system and broadband optical transduction. Our broadband optomechanical transduction model, in conjunction with spatially resolved motion power spectral data, closely predicts the change in optomechanical coupling strength of the LGPRs. These results can form the basis of a useful design space for future plasmomechanical systems whereby a desired optomechanical response (e.g., dispersive or reactive coupling, enhancement or suppression of signals at certain frequencies) can be engineered into the system through felicitous “decoration” of the mechanical system with subwavelength optical resonators. By making such features available, we envision that this work will benefit future applications of plasmomechanical systems in metrology, nanomechanical sensing and signal processing and extend these capabilities to future white-light optomechanics using incoherent sources.

Methods

Device fabrication. Devices are fabricated using a procedure detailed previously[23]. Briefly, the process uses repeated steps of electron beam lithography (EBL) for patterning. The bottom pads are formed by electron beam evaporation and liftoff (EBEL) of a Ti-Au-Cr stack with thicknesses of approximately 5 nm, 50 nm, and 15 nm. Next, the ≈ 40 nm thick cuboids are formed using aligned EBL and EBEL. The silicon nitride layer measuring ≈ 150 nm is deposited using plasma enhanced chemical vapor deposition (PECVD), followed by two additional steps of EBL and EBEL to form the Au actuators and leads, each having a ≈ 5 Ti layer underneath for adhesion. A final aligned EBL with reactive ion etching is used to pattern the silicon nitride cantilevers, followed by a wet chemical etch of Cr and critical point drying to release the devices. The devices are wirebonded onto a printed circuit board to facilitate electrostatic via an applied radio-frequency voltage.

Controlling the stress gradient in the deposited nitride film is a crucial process step as it simultaneously determines (i) whether or not the cantilever will remain suspended following the release and (ii) the final deflected shape of the cantilever. It has been previously shown [23] that as the initial gap is decreased (a thinner Cr layer as deposited), larger stress gradients are needed to overcome attractive forces that tend to collapse the cantilever to the Au substrate (stiction). We control the residual stress and stress gradient [31] by modifying both the radio frequency (RF) and the inductively coupled plasma

(ICP) power supplied during our PECVD process; the residual stress being directly proportional to the input power of both sources. For a desired initial gap, test samples are produced with varying RF and ICP power to determine a combination that ensures release yet produces the minimum device curvature. We find that an RF and ICP power settings of 100 W and 1200 W produces a residual compressive stress of approximately -200 MPa and a sufficient stress gradient through our approximately 150 nm thick film to ensure released devices.

Acknowledgements
The authors thank B. Ilic and M. Pruessner for a meticulous reading of the manuscript and fruitful discussions.

Author Contributions
B.J. Roxworthy designed and fabricated the devices, performed the modelling, simulations, and experiments, analyzed the results and co-wrote the manuscript. S. Vangara performed proof of principle experiments and analyzed the results. V.A. Aksyuk designed the devices, performed the simulations, analyzed the results and co-wrote the manuscript.

References

(1) Giessibl, F. J. Advances in Atomic Force Microscopy. *Rev. Mod. Phys.* **2003**, *75*, 949–983.
(2) Hanay, M. S.; Kelber, S. I.; O'Connell, C. D.; Mulvaney, P.; Sader, J. E.; Roukes, M. L. Inertial Imaging with Nanomechanical Systems. *Nat. Nanotechnol.* **2015**, *10*, 339–344.
(3) Ilic, B.; Craighead, H. G.; Krylov, S.; Senaratne, W.; Ober, C.; Neuzil, P. Attogram Detection Using Nanoelectromechanical Oscillators. *J. Appl. Phys.* **2004**, *95*, 3694–3703.
(4) Chaste, J.; Eichler, A.; Moser, J.; Ceballos, G.; Rurali, R.; Bachtold, A. A Nanomechanical Mass Sensor with Yoctogram Resolution. *Nat. Nanotechnol.* **2012**, *7*, 301–304.
(5) Arlett, J. L.; Myers, E. B.; Roukes, M. L. Comparative Advantages of Mechanical Biosensors. *Nat. Nanotechnol.* **2011**, *6*, 203–215.
(6) Bagci, T.; Simonsen, A.; Schmid, S.; Villanueva, L. G.; Zeuthen, E.; Appel, J.; Taylor, J. M.; Sørensen, A.; Usami, K.; Schliesser, A.; et al. Optical Detection of Radio Waves through a Nanomechanical Transducer. *Nature* **2014**, *507*, 81–85.
(7) Verhagen, E.; Deléglise, S.; Weis, S.; Schliesser, A.; Kippenberg, T. J. Quantum-Coherent Coupling of a Mechanical Oscillator to an Optical Cavity Mode. *Nature* **2012**, *482*, 63–67.
(8) O'Connell, A. D.; Hofheinz, M.; Ansmann, M.; Bialczak, R. C.; Lenander, M.; Lucero, E.; Neeley, M.; Sank, D.; Wang, H.; Weides, M.; et al. Quantum Ground State and Single-Phonon Control of a Mechanical Resonator. *Nature* **2010**, *464*, 697–703.
(9) Ekinci, K. L.; Roukes, M. L. Nanoelectromechanical Systems. *Rev. Sci. Instrum.* **2005**, *76*, 061101.
(10) Srinivasan, K.; Miao, H.; Rakher, M. T.; Davanço, M.; Aksyuk, V. Optomechanical Transduction of an Integrated Silicon Cantilever Probe Using a Microdisk Resonator. *Nano Lett.* **2011**, *11*, 791–797.
(11) Kouh, T.; Hanay, M. S.; Ekinci, K. L. Nanomechanical Motion Transducers for Miniaturized Mechanical Systems. *Micromachines* **2017**, *8*, 108.
(12) Aspelmeyer, M.; Kippenberg, T. J.; Marquardt, F. Cavity Optomechanics. *Rev. Mod. Phys.* **2014**, *86*, 1391–1452.
(13) Teufel, J. D.; Donner, T.; Castellanos-Beltran, M. A.; Harlow, J. W.; Lehnert, K. W. Nanomechanical Motion Measured with Precision beyond the Standard Quantum Limit. *Nat. Nanotechnol.* **2009**, *4*, 820–823.
(14) Ou, J. Y.; Plum, E.; Jiang, L.; Zheludev, N. I. Reconfigurable Photonic Metamaterials. *Nano Lett.*

2011, *11*, 2142–2144.
(15) Thijssen, R.; Verhagen, E.; Kippenberg, T. J.; Polman, A. Plasmon Nanomechanical Coupling for Nanoscale Transduction. *Nano Lett.* **2013**, *13*, 3293–3297.
(16) Thijssen, R.; Kippenberg, T. J.; Polman, A.; Verhagen, E. Plasmomechanical Resonators Based on Dimer Nanoantennas. *Nano Lett.* **2015**, *15*, 3971–3976.
(17) Roxworthy, B. J.; Aksyuk, V. A. Nanomechanical Motion Transduction with a Scalable Localized Gap Plasmon Architecture. *Nat. Commun.* **2016**, *7*, 13746.
(18) Zhu, H.; Yi, F.; Cubukcu, E. Plasmonic Metamaterial Absorber for Broadband Manipulation of Mechanical Resonances. *Nat. Photonics* **2016**, *10*, 709–714.
(19) Miyata, M.; Holsteen, A.; Nagasaki, Y.; Brongersma, M. L.; Takahara, J. Gap Plasmon Resonance in a Suspended Plasmonic Nanowire Coupled to a Metallic Substrate. *Nano Lett.* **2015**, *15*, 5609–5616.
(20) Dong, B.; Chen, X.; Zhou, F.; Wang, C.; Zhang, H. F.; Sun, C. Gigahertz All-Optical Modulation Using Reconfigurable Nanophotonic Metamolecules. *Nano Lett.* **2016**, *16*, 7690–7695.
(21) Dennis, B. S.; Haftel, M. I.; Czaplewski, D. A.; Lopez, D.; Blumberg, G.; Aksyuk, V. A. Compact Nanomechanical Plasmonic Phase Modulators. *Nat. Photonics* **2015**, *9*, 267–273.
(22) Imade, Y.; Ulbricht, R.; Tomoda, M.; Matsuda, O.; Seniutinas, G.; Juodkazis, S.; Wright, O. B. Gigahertz Optomechanical Modulation by Split-Ring-Resonator Nanophotonic Meta-Atom Arrays. *Nano Lett.* **2017**, *17*, 6684–6689.
(23) Roxworthy, B. J.; Aksyuk, V. A. Electrically Tunable Plasmomechanical Oscillators for Localized Modulation, Transduction, and Amplification. *Optica* **2018**, *5*, 71–79.
(24) Ou, J. Y.; Plum, E.; Zhang, J.; Zheludev, N. I. Giant Nonlinearity of an Optically Reconfigurable Plasmonic Metamaterial. *Adv. Mater.* **2016**, *28*, 729–733.
(25) Li, M.; Pernice, W. H. P.; Tang, H. X. Broadband All-Photonic Transduction of Nanocantilevers. *Nat. Nanotechnol.* **2009**, *4*, 377–382.
(26) Bozhevolnyi, S. I.; Søndergaard, T. General Properties of Slow-Plasmon Resonant Nanostructures: Nano-Antennas and Resonators. *Opt. Express* **2007**, *15*, 10869–10877.
(27) Wu, M.; Hryciw, A. C.; Healey, C.; Lake, D. P.; Jayakumar, H.; Freeman, M. R.; Davis, J. P.; Barclay, P. E. Dissipative and Dispersive Optomechanics in a Nanocavity Torque Sensor. *Phys. Rev. X* **2014**, *4*, 021054.
(28) Li, M.; Pernice, W. H. P.; Tang, H. X. Reactive Cavity Optical Force on Microdisk-Coupled Nanomechanical Beam Waveguides. *Phys. Rev. Lett.* **2009**, *103*, 223901.
(29) Anetsberger, G.; Weig, E. M.; Kotthaus, J. P.; Kippenberg, T. J. Cavity Optomechanics and Cooling Nanomechanical Oscillators Using Microresonator Enhanced Evanescent Near-Field Coupling. *Comptes Rendus Phys.* **2011**, *12*, 800–816.
(30) Jain, P. K.; Huang, W.; El-Sayed, M. A. On the Universal Scaling Behavior of the Distance Decay of Plasmon Coupling in Metal Nanoparticle Pairs: A Plasmon Ruler Equation. *Nano Lett.* **2007**, *7*, 2080–2088.
(31) Chinthakindi, A. K.; Kohl, P. a. Electrostatic Actuators with Intrinsic Stress Gradient. *J. Electrochem. Soc.* **2002**, *149*, H139–H145.
(32) Bao, M.; Yang, H. Squeeze Film Air Damping in MEMS. *Sensors Actuators, A Phys.* **2007**, *136*, 3–27.
(33) Foreman, M. R.; Török, P. Computational Methods in Vectorial Imaging. *J. Mod. Opt.* **2011**, *58*, 339–364.
(34) Hauer, B. D.; Doolin, C.; Beach, K. S. D.; Davis, J. P. A General Procedure for Thermomechanical Calibration of Nano/Micro-Mechanical Resonators. *Ann. Phys.* **2013**, *339*, 181–207.
(35) Roxworthy, B. J.; Bhuiya, A. M.; Inavalli, V. V. G. K.; Chen, H.; Toussaint, K. C. Multifunctional Plasmonic Film for Recording Near-Field Optical Intensity. *Nano Lett.* **2014**, *14*, 4687–4693.

(36) Inasawa, S.; Sugiyama, M.; Yamaguchi, Y. Laser-Induced Shape Transformation of Gold Nanoparticles below the Melting Point: The Effect of Surface Melting. *J. Phys. Chem. B* **2005**, *109*, 3104–3111.

For Table of Contents Use Only